Editors' Suggestion

Magnetic order and Li diffusion in the $\frac{1}{3}$-filled kagome layers of the antiperovskite lithium-ion battery materials $(Li_2Fe)SO$ and $(Li_2Fe)SeO$

F. Seewald [1], T. Schulze [2,3], N. Gräßler [2], F. L. Carstens [4], L. Singer [4], M. A. A. Mohamed [2,5], S. Hampel [2], B. Büchner [2,3], R. Klingeler [4,*], H.-H. Klauss [1,†] and H.-J. Grafe [2,‡]

[1] *Institut für Festkörperphysik, Technische Universität Dresden, 01062 Dresden, Germany*

[2] *Leibniz Institute for Solid State and Materials Research Dresden, 01069 Dresden, Germany*

[3] *Technische Universität Dresden, 01062 Dresden, Germany*

[4] *Kirchhoff Institute for Physics, Heidelberg University, INF 227, D-69120 Heidelberg, Germany*

[5] *Department of Physics, Faculty of Science, Sohag University, 82524 Sohag, Egypt*

(Received 25 April 2025; revised 30 June 2025; accepted 20 August 2025; published 22 September 2025)

The recently discovered lithium-rich antiperovskites $(Li_2Fe)SeO$ and $(Li_2Fe)SO$ host lithium and iron ions on the same atomic position which octahedrally coordinates to central oxygens. In a cubic antiperovskite these sites form kagome planes stacked along the ⟨111⟩ directions which triangular motifs induce high geometric frustration in the diluted magnetic sublattice for antiferromagnetic interactions. Despite their compelling properties as high-capacity Li-ion battery cathode materials, very little is known about the electronic and magnetic properties of lithium-rich antiperovskites. We report static magnetization, Mössbauer, and NMR studies on both compounds. Our data reveal a Pauli paramagnetic-like behavior, a long-range antiferromagnetically ordered ground state below ≈50 K, and a regime of short-range magnetic correlations up to 100 K. Our results are consistent with a random Li-Fe distribution on the shared lattice position. In addition, Li-hopping is observed above 200 K with an activation energy of $E_a = 0.47$ eV. Overall, our data elucidate static magnetism in a disordered magnetically frustrated and presumably semimetallic system with thermally induced ion diffusion dynamics.

DOI: 10.1103/t7tf-5ntl

I. INTRODUCTION

Lithium transition metal (TM) oxides are standard electrode materials for Li-ion batteries (LIBs) (see, e.g., Refs. [1,2] and references therein). For their functionality the Li diffusion properties and Li intercalation capacity at room temperature and above are essential. Li-rich antiperovskite materials are promising candidates in this context (see, e.g., Ref. [3]). Recently, the class of $(Li_2Fe)ChO$ (Ch = S, Se, Te) has been found [4–6] and their feasibility as electrode materials in LIBs has become a current research topic in battery research.

Li-rich antiperovskites possess cubic crystal structures (space group $Pm\bar{3}m$ [4]) as sketched in Fig. 1(a), in which lithium and iron ions occupy the same lattice position (3c) with 2/3 and 1/3 probability, respectively. Since Li^+ and Fe^{2+} are too small for their common atomic position they exhibit large thermal displacements, implying a high cation mobility [4] which is a prerequisite for their use in LIBs. In theoretical studies of $(Li_2Fe)SO$ a thermally activated Li-diffusion with a very small diffusion barrier of 0.32 eV was deduced [5]. For ionic diffusion, disorder can have dramatic effects. In most Li-TM oxides disorder is caused by various defects which indeed have an enormous effect on Li diffusion by blocking or enabling low-energy ionic pathways [7–9] and on magnetism [10–14]. In contrast, randomness is much more pronounced in Li-rich antiperovskites due to the shared Li-TM position. It produces long-range disorder, yet a preferential oxygen coordination has been recently suggested to stabilize polar short-range cation orderings [15,16].

From the viewpoint of fundamental research in magnetism, the presumably largely random distribution of diamagnetic and paramagnetic species on the same lattice site render Li-rich antiperovskites model systems to study magnetism and the potential evolution of long-range magnetic order in a disordered semimetal. The TM sites in antiperovskites exhibit kagome planes stacked along the ⟨111⟩ directions [see Fig. 1(b)] [17]. Therefore, for nearest-neighbor antiferromagnetic interaction strong magnetic frustration on triangular units is expected. Since the kagome planes exist along all ⟨111⟩ directions, this is not a two-dimensional but an isotropic three-dimensional magnetic system. No macroscopic magnetic ground-state degeneracy is expected.

In this work we identify and characterize $(Li_2Fe)SeO$ and $(Li_2Fe)SO$ with respect to magnetic order of the Fe moments and examine if the Li and Fe ions are indeed statistically distributed on the shared lattice site. Moreover we search for signatures of Li diffusion in ^{7}Li NMR spectroscopy and evaluate the experimental energy barrier for Li diffusion, which is determined as $E_a \simeq 0.47$ eV. Notably, long-range antiferromagnetic order is observed in our macroscopic and local probe studies which in particular enable us to determine the temperature dependence of the

*Contact author: klingeler@kip.uni-heidelberg.de
†Contact author: henning.klauss@tu-dresden.de
‡Contact author: H.Grafe@ifw-dresden.de

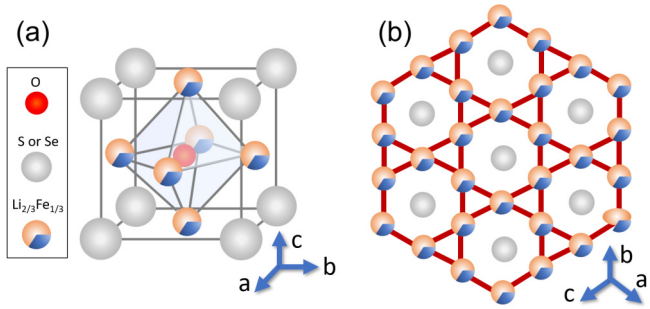

FIG. 1. (a) Schematics of the crystallographic unit cell of $(Li_2Fe)ChO$ (Ch = Se or S) (after Ref. [4]). 1/3 (2/3) of the crystallographic 3c sites of the $Pm\bar{3}m$ structure are filled with paramagnetic Fe (diamagnetic Li) species. (b) View along the ⟨111⟩ direction; red lines between the 3c sites illustrate the underlying kagome layers.

magnetic order parameter. While long-range antiferromagnetic order appears below 50 K, short-range order is observed up to ≈100 K. This reflects the strong dilution of the iron ions on the TM site as well as the partly lifted geometric frustration of the antiferromagnetic nearest-neighbor magnetic exchange interaction within the kagome planes. The geometric frustration manifests itself also in a nonlinear dependence of the ^{57}Fe magnetic hyperfine field on the number n of nearest-neighbor Fe ions in the long-range ordered state.

II. EXPERIMENTAL METHODS

The $(Li_2Fe)SO$ and $(Li_2Fe)SeO$ samples were synthesized by ball milling (BM) [18]. In addition to investigating the pristine materials, postsynthesis annealing was carried out to further reduce impurity phases. Sulfur-containing samples were heat-treated at 300 °C and 500 °C, while selenium-containing samples were annealed at 600 °C [19]. Details of the synthesis as well as a detailed characterization of the $(Li_2Fe)SO$ and $(Li_2Fe)SeO$ samples studied at hand can be found in Refs. [18,20]. The corresponding x-ray diffraction (XRD) patterns are shown in the Appendix (see Fig. 13).

The samples have been stored in glass tubes sealed by Teflon® dumplings in an argon-filled glovebox with controlled humidity and oxygen concentration due to the moisture sensitivity of Li_2FeChO. For the magnetometry, Mössbauer, and NMR experiments, appropriate amounts of the powder samples were filled in glass tubes or plastic containers sealed by Teflon® within the glovebox. These were quickly transferred into the MPMS, Mössbauer and NMR cryostats, where the samples were measured under a He atmosphere also at high temperatures.

Magnetic measurements were performed on powder samples using an MPMS3 magnetometer (Quantum Design). The static magnetic susceptibility $\chi = M/B$ was obtained upon varying the temperature at 1 T by using field-cooled (FC) and zero-field-cooled (ZFC) protocols, where the sample was cooled either in the external measurement field or the field was applied after cooling to the lowest temperature. Isothermal magnetization $M(B)$ was measured at $T = 1.8$ K in the field range $-7\ \mathrm{T} \leqslant B \leqslant +7\ \mathrm{T}$.

^{57}Fe-Mössbauer measurements were conducted in a CryoVac flow cryostat under He atmosphere. A Rh/Co source driven by a Mössbauer WissEL drive unit MR-360 biased by a DFG-500 frequency generator in sinusoidal mode was used. The detection device is a proportional counter tube in combination with a multichannel data processor CMTE MCD 301/8K and a WissEL single channel analyzer Timing SCA to set the energy window. Powder samples of $(Li_2Fe)SO$ and $(Li_2Fe)SeO$ were investigated. All data evaluation was performed using MOESSFIT [21], using the implemented maximum entropy method (MEM) to describe fit parameter distributions. Measurements were carried out between 4.2 and 300 K. All center shifts are stated relative to room temperature α-Fe. The linewidth ω is given as half width at half maximum (HWHM).

^{7}Li NMR has been measured in an external magnetic field of $2.001T$. Due to a gyromagnetic ratio of $\gamma = 16.5471$ MHz/T for the ^{7}Li isotope the resonance frequency for the bare nucleus is 33.11 MHz. The ^{7}Li spectra were taken by the Hahn-spin-echo sequence. Since the spectra broaden at low temperatures, we applied a step-and-sum technique, i.e., we measured spectra while stepping the frequency in 50 kHz steps and added the Fourier-transformed spectra taken at each step. The spin-lattice relaxation time T_1 was measured at the peak position of the spectra by a saturation recovery sequence using a train of 90° pulses at a time t before a Hahn-spin-echo sequence. The spin-spin relaxation time T_2 was measured at the peak of the spectra by varying the time τ between the 90° and the 180° pulse of the Hahn-spin-echo sequence.

III. RESULTS AND DISCUSSION

A. Magnetic susceptibility and magnetization

In Fig. 2 we depict the static magnetic susceptibility $\chi(T) = M(T)/B$ using zero-field cooled (ZFC) and field cooled (FC) protocols as well as isothermal magnetization measurements $M(B)$ of two samples of $(Li_2Fe)SeO$ (as-grown and with postsynthesis 600 °C heat treatment, respectively) and two samples of $(Li_2Fe)SO$ (as grown and with 500 °C heat treatment). In the ZFC data, all samples exhibit a maximum in $\chi(T)$ as well as an FC-ZFC splitting. Upon heating between 100 and 300 K we find a nearly constant or weakly decreasing (typically by 5%) magnetic susceptibility which is typically associated with strong Pauli paramagnetism of 3d conduction electrons. Below 100 K all samples exhibit an increase of $\chi(T)$ which—by comparison with the local probe data presented below—we attribute to the onset of short-range magnetic correlations. We suspect this to be iron and Fe_xS with $x \leqslant 1$ which has been detected in x-ray diffraction and Mössbauer spectroscopy. The presence of ferromagnetic impurity phases yields a small offset in the χ vs T curves as well as the corresponding magnetization steps at zero external field in the magnetization measurements (see insets of Fig. 2). From the anomalies in the magnetization we deduce ferromagnetic minority phases with typical 0.1% volume fraction, only the pristine $(Li_2Fe)SO$ sample showed a ferromagnetic minority phases with 2% volume fraction (see also Appendix A). A nearly temperature-independent magnetic susceptibility, however at five times larger absolute values

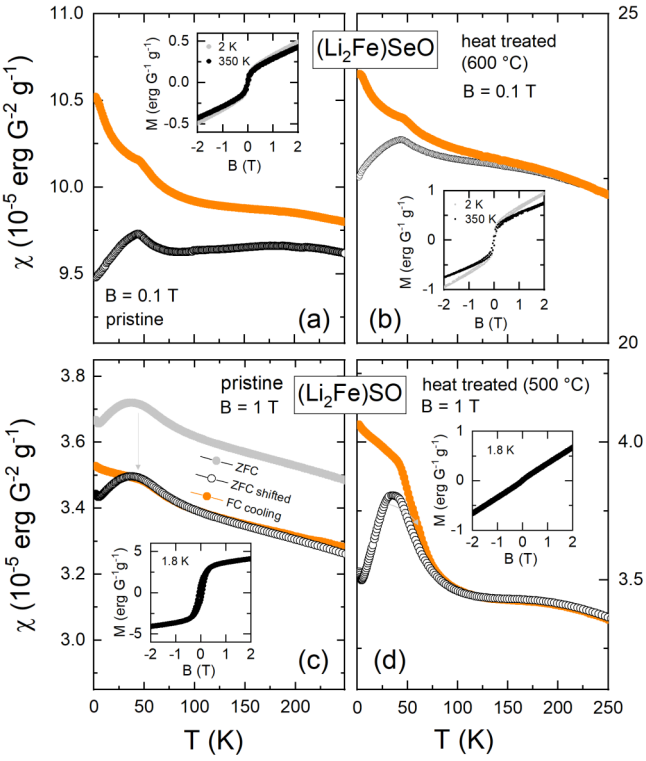

FIG. 2. Static magnetic susceptibility ($\chi = M/B$) of (a), (b) $(Li_2Fe)SO$ and (c), (d) $(Li_2Fe)SeO$ vs temperature up to 250 K. Both FC (filled orange markers) and ZFC (open black markers) protocols have been applied. Panels (a), (c) show pristine materials and panels (b), (d) show postsynthesis heat-treated materials. In panel (c), the ZFC data (gray) have been shifted (black) to compensate for a hysteresis effect of a small ferromagnetic impurity phase. Insets show the corresponding isothermal magnetization.

of χ and without clear low-temperature features as observed here, has been reported for a $(Li_2Fe)SO$ sample with larger ferromagnetic, possibly Fe_3O_4, impurity contents [19,22]. The effect of heat-treatment on reducing and eliminating such magnetic impurity phases in $(Li_2Fe)SO$ is discussed in Refs. [18,19].

The FC measurements of the heat-treated materials allow us to further investigate the evolution of magnetic order by considering Fisher's specific heat $\partial(\chi T)/\partial T$ which is derived from the static magnetic susceptibility data. This quantity is proportional to the magnetic specific heat [23]. In both materials, Fisher's specific heat indicates a broad regime of magnetic entropy changes extending from $\simeq$30 K to above 100 K (see Fig. 3). In $(Li_2Fe)SeO$ as well as in $(Li_2Fe)SO$, a step-like feature appears at around 50 K which indicates a magnetic phase transition. As will be shown by our local probe data below (e.g., documented by the appearance of static magnetic hyperfine fields at the ^{57}Fe nuclei below 60 K in Fig. 4), this feature is associated with a long-range antiferromagnetic order transition of the Fe moments. Towards lower temperatures, the step in the magnetic specific heat is contained by a tiny maximum respectively a kink at $\simeq$44 K marked by T^* in Fig. 3. We also note the existence of a minimum in $\partial(\chi T)/\partial T$ for $(Li_2Fe)SO$ at 65 K which indicates a precursing magnetically ordered phase [24].

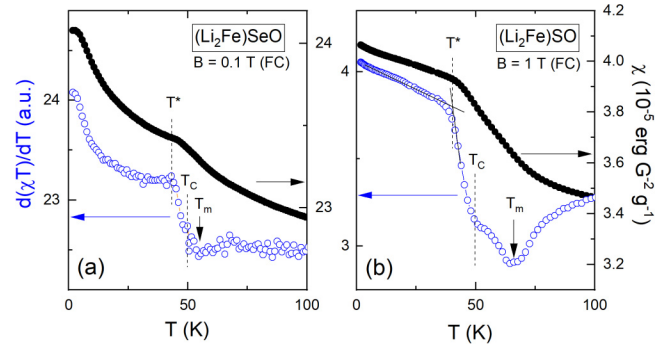

FIG. 3. Fisher's specific heat $\partial(\chi T)/\partial T$ (blue open markers) as derived from the field cooled static magnetic susceptibility (black filled markers) in Figs. 2(b) and 2(d). The shoulder or minimum feature marked by T_C signals the evolution of long-range magnetic order as evinced by the local probe data (see Fig. 8). T^* marks a kink and T_m a further minimum in Fisher's specific heat (see the text).

B. Mössbauer spectroscopy

Figure 4 depicts selected ^{57}Fe-Mössbauer powder spectra of $(Li_2Fe)SO$ and $(Li_2Fe)SeO$. At room temperature the spectra of both samples can be described with a single main iron site exhibiting quadrupole splitting due to a finite electric field gradient (EFG) at the ^{57}Fe nucleus. Below 60 K the spectra broaden and six absorption lines develop and document the gradual appearance of an additional static magnetic hyperfine field at the ^{57}Fe nucleus. As will be discussed in detail below the magnetic hyperfine field distribution is not homogeneous and single-valued yet broadened due to the probability distribution of the number of Fe-Fe neighbors on the Fe site. Except a minor precursor observed for $(Li_2Fe)SO$ at 55 K the onset and continuous increase of static magnetic hyperfine fields for the full spectrum is observed in both systems at 50 K and below. This order-parameter-like increase (see Fig. 8) proves a magnetic phase transition into a magnetically long-range ordered state.

At room temperature the spectra of both samples can be described with a single main iron site exhibiting quadrupole splitting, as seen in Fig. 5. The HWHM linewidth is determined to 0.218(16) mm s^{-1} for $(Li_2Fe)SO$ and 0.184(16) mm s^{-1} for $(Li_2Fe)SeO$. These values are enhanced only by $\approx$0.05 to 0.1 mm s^{-1} with respect to the natural linewidth in the ^{57}Fe Mössbauer experiment. We conclude that there is only a very small variation of the electrostatic quadrupole interaction due to different nearest-neighbor lithium-iron configurations. In our analysis this effect is absorbed into the HWHM linewidth as a global parameter at all temperatures. Assuming an EFG with principal components $\|V_{zz}\| \geqq \|V_{yy}\| \geqq \|V_{xx}\|$ and an asymmetry of $\eta = (V_{xx} - V_{yy})/V_{zz} = 0$ the value obtained for the main principle component V_{zz} is $V_{zz} = 65.72(20)$ V Å^{-2} and $V_{zz} = 62.7(12)$ V Å^{-2} for the sulfur and selenium samples, respectively. In $(Li_2Fe)SO$ a temperature-dependent asymmetry between the two peaks as well as pronounced shoulders are observed in addition to the main powder site. To describe the significant asymmetry of the doublet observed for the sulfur sample an additional doublet with 16.4(14)% spectral area, an EFG principle component of $V_{zz} = 62.2(25)$ V Å^{-2}, and a center shift of 0.313(20) mm s^{-1}

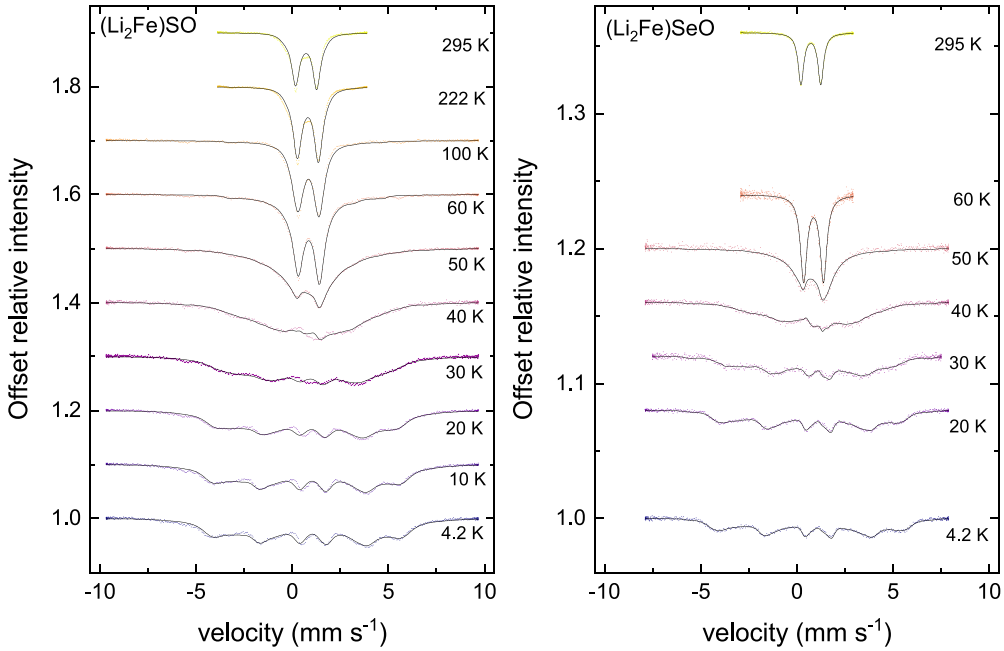

FIG. 4. Mössbauer spectra of $(Li_2Fe)SO$ and $(Li_2Fe)SeO$ between 4.2 and 295 K. Below 60 K the onset of static magnetic order is documented by a spectral broadening and the gradual appearance of a six line magnetic hyperfine field splitting.

is used. This can be associated with Fe_xS with $x \leqslant 1$ or $LiFeO_2$ which have been detected as minority phases in XRD. The shoulders at ≈ -3 mm s^{-1} and $+2.5$ mm s^{-1} could be associated with a small volume (less than 5%) FeS magnetic impurity phase.

At 4.2 K both samples show inhomogeneously broadened sextets proving the presence of local magnetic hyperfine fields B_{hyp} at the iron positions (see Fig. 6). The strongly increased linewidth with respect to the nonmagnetic high-temperature spectra can be attributed to a distribution of hyperfine fields at different iron atoms. Figure 7 presents the measured distribution of local hyperfine fields at 4.2 K, with the median values of 26.25 T for the sulfur sample and 24.75 T for the selenium sample. The spectra are deduced from a maximum entropy method (MEM) analysis with a B_{hyp} resolution of 0.5 T. The observation of a hyperfine field distribution is consistent with Li-Fe disorder on the shared lattice position since this leads to a variety of local iron environments with varying numbers of nearest-iron neighbors.

Figure 7 also depicts two calculated hyperfine field distributions. Recent x-ray pair distribution function (PDF) studies have shown a nearly random occupation of the Li-Fe shared lattice position [15,16]. Each iron has eight nearest-TM neighbors with $2/3$ lithium and $1/3$ iron occupancy. Table I displays the relative probabilities f_n for n Fe-O-Fe neighborhoods assuming a random lithium-iron distribution given by

$$f_n = \frac{8!}{(8-n)!n!}\left(\frac{1}{3}\right)^n\left(\frac{2}{3}\right)^{8-n}. \tag{1}$$

The Fe magnetic hyperfine field is proportional to the local magnetic exchange field at the Fe ion. To model the distribution we consider the number of Fe nearest and next-nearest neighborships in the lattice. Due to the disordered nature of the magnetic lattice we assume that local superexchange interactions dominate. The eight nearest neighborships involve a 60° antiferromagnetic exchange via two (S,Se) ions and a weak ferromagnetic 90° exchange via an oxygen ion. Due to the antiferromagnetic character of the long-range magnetic transition at ≈50 K we consider an effective antiferromagnetic exchange with the eight nearest-neighbor Fe ions. In an unfrustrated magnetic lattice the resulting local hyperfine field scales with the number n of Fe neighbors, i.e., $B(n) = B_0 n$ with B_0 being a scaling parameter of the hyperfine field chosen to match the experimental maximum. B_0 and the corresponding fraction f_n obtained from Eq. (1) define the area of the corresponding rectangle in Fig. 7. The resulting hyperfine field distribution is plotted in blue. This distribution shows a broad high-field shoulder not seen in the experimental spectrum. A possible interpretation would be that Fe-Fe configurations with five, six, or seven nearest neighbors are not realized and the random Li-Fe distribution assumption (in which approximately 9% Fe sites are expected for these configurations) is not realized. However, this would contradict the interpretation of recent x-ray PDF studies [15,16].

Considering that the dominant local magnetic exchange geometry is triangular with strong geometric frustration for antiferromagnetic exchange, the local magnetic exchange field observed via the Fe magnetic hyperfine field is not linear in the number n of nearest neighbors but exhibits a saturation for increasing n. Therefore, we model $B(n)$ using the phenomenological ansatz

$$B(n) = B_0 \sum_{i=1}^{n} \frac{1}{i}, \tag{2}$$

in which the contribution of each additional nearest-neighbor i will increase the total exchange field by a contribution proportional to $1/i$. The resulting hyperfine field distribution (red color in Fig. 7) describes the asymmetric experimental

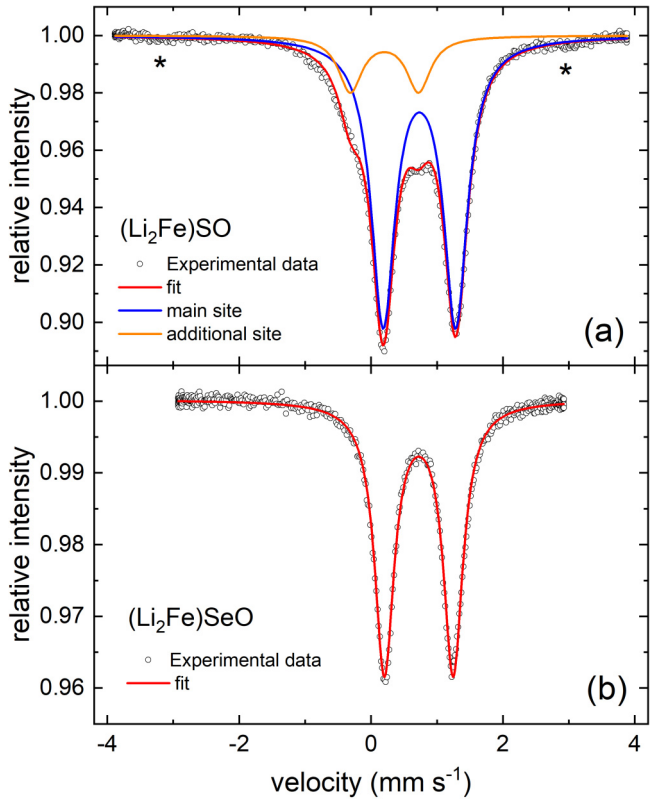

FIG. 5. Mössbauer spectrum of (a) $(Li_2Fe)SO$ and (b) $(Li_2Fe)SeO$ at room temperature. For $(Li_2Fe)SO$, in addition to the main site, a second quadrupole-split doublet with hyperfine parameters similar to Fe_x and α-$LiFeO_2$ is modeled to account for the main doublet asymmetry. Moreover, two weak magnetic absorption lines are observed at -3.2 mm s^{-1} and $+2.8$ mm s^{-1} marked by asterisks, which are associated with a $<5\%$ α-iron impurity. The $(Li_2Fe)SeO$ spectrum is described by a single quadrupole-split site.

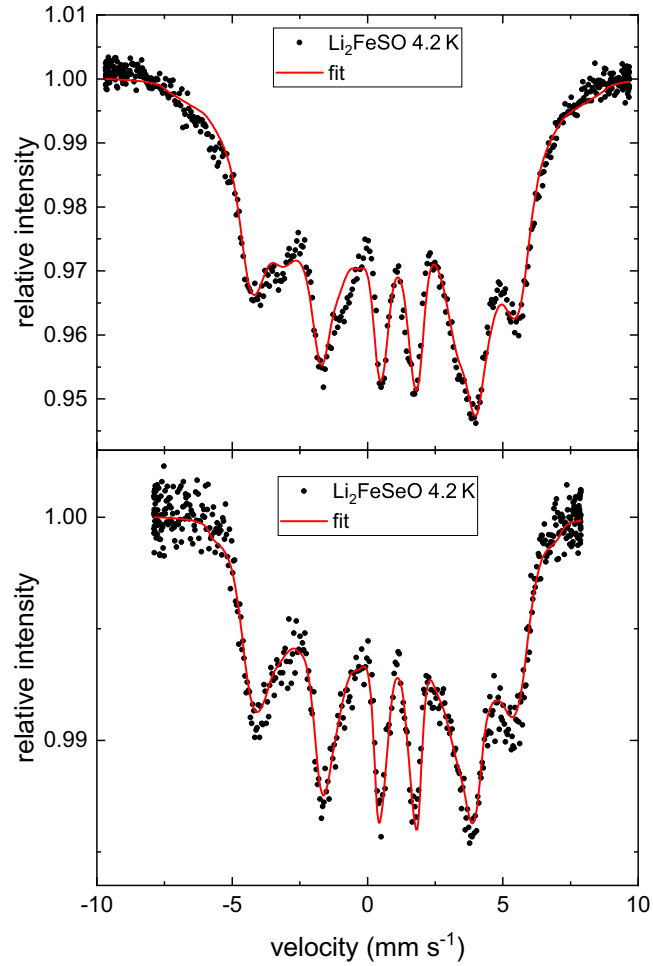

FIG. 6. Mössbauer spectrum of $(Li_2Fe)SO$ (upper panel) and $(Li_2Fe)SeO$ (lower panel) at 4.2 K. A magnetic sextet with broad lines is observed and modeled by a hyperfine field distribution.

spectrum in $(Li_2Fe)SO$ and $(Li_2Fe)SeO$ at 4.2 K much better than the linear model.

Note that, in this figure, we also include a contribution from the 3.9% Fe sites, which have no nearest Fe neighbor but may experience an exchange field due to second-nearest Fe neighbors. The presence of such higher-order-interaction terms is indeed suggested by the fact that our $M(B)$ data of thermally treated $(Li_2Fe)SO$ implies only an insignificant amount of quasifree moments, i.e., obeying a Brillouin-like behavior, in the 1% regime [see Fig. 2(d)]. For the Fe sites without nearest paramagnetic neighbors we assume a flat field distribution in the field range between 0 T and the onset field value of the model distribution for finite numbers of nearest Fe neighbors.

The MEM fit model can be employed to describe the spectra at all temperatures. Figure 8 shows the temperature-dependent median magnetic hyperfine fields $B_{\mathrm{hyp}}^{\mathrm{median}}$ following a $B_{\mathrm{hyp}} = B_0[1 - (\frac{T}{T_c})^{\alpha}]^{\beta}$ behavior with $\alpha = 2.2(4)$ and $\beta = 0.56(11)$ [25]. This phenomenological model is adapted to the data assuming identical T_C, α, and β for both samples scaled by independent low-temperature saturation values $B_0 = 26.54(38)$ T $[(Li_2Fe)SO]$ and $B_0 = 25.1(5)$ T $[(Li_2Fe)SeO]$. In this model β is the usual critical exponent of the order parameter in the Wilson renormalization-group theory describing the decrease close to the critical temperature and α describes the change of the order parameter close to $T = 0$ K. Hence, the deduced value for β is consistent with 0.5 which is the mean-field value, and α is slightly smaller than three, which is the exponent for the Bloch long-wavelength magnon-induced order-parameter decrease for antiferromagnets close to $T = 0$.

For the selenium sample, $B_{\mathrm{hyp}}^{\mathrm{median}}$ tends towards zero above 50 K and spectra recorded at $T = 55$ K and above are compatible with setting the maximum hyperfine field to zero. For the sulfur sample $B_{\mathrm{hyp}}^{\mathrm{median}}$ tends to zero between 55 and 60 K. This observation corresponds to the minimum in Fisher's specific heat, which indicates an anomaly in the magnetic entropy changes at 65 K (see Fig. 3). Such a feature above T_C is absent in the Fisher specific heat of $(Li_2Fe)SeO$. As depicted in Fig. 5 (upper panel), a small fraction of iron nuclei (less than 5%) experiences a nonzero local magnetic hyperfine field up to room temperature. This can be associated with an α-iron impurity phase.

Introducing the angle θ between the local hyperfine field and the principle EFG component as a free parameter enables us to describe the data with global values for θ and V_{zz}

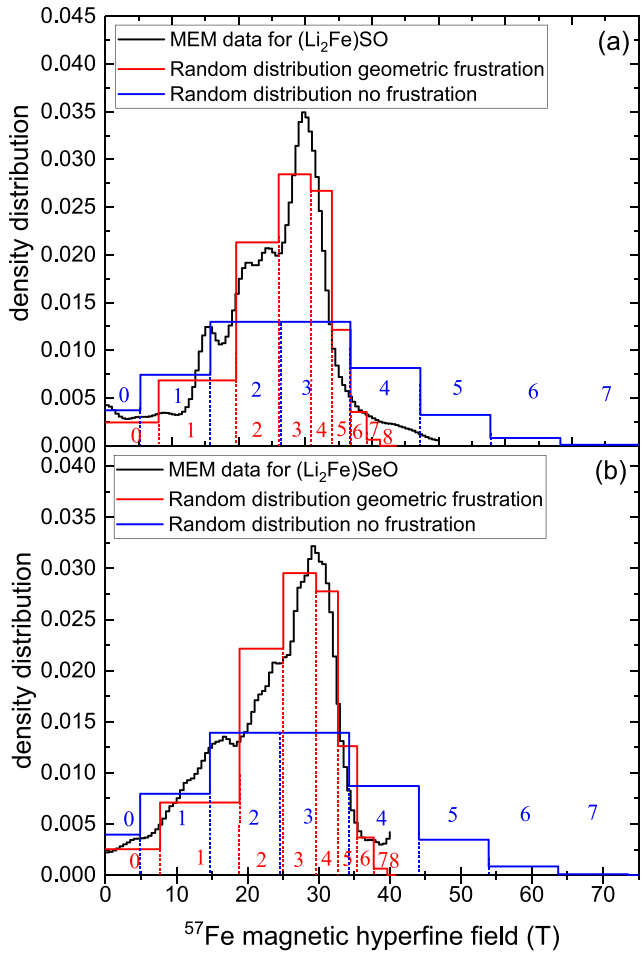

FIG. 7. (black lines) Measured magnetic hyperfine field probability distribution ρ in $(Li_2Fe)SO$ (a) and $(Li_2Fe)SeO$ (b) at 4.2 K compared with two different models assuming a random distribution of iron and lithium ions on the shared lattice site: (blue lines) linear model (unfrustrated exchange), (red lines) frustrated exchange model with $B(i) \propto 1/i$. All probability distributions are normalized to a total area of 1. Blue and red numbers indicate the number i of nearest-neighbor iron ions for the two models.

shared for all temperatures. For the sulfur sample we obtain $V_{zz,\mathrm{global}} = 65.13$ V Å^{-2} and $\theta_{\mathrm{global}} = 68.59°$, and $V_{zz,\mathrm{global}} = 61.97$ V Å^{-2} and $\theta_{\mathrm{global}} = 79.73°$ for the selenium sample. In this model the angle θ_{global} is an effective angle averaged over different local iron environments due to the iron-lithium disorder.

C. NMR results

1. Analysis of NMR spectra

^{7}Li NMR spectra of polycrystalline $(Li_2Fe)SO$ and $(Li_2Fe)SeO$ are shown in Fig. 9 for temperatures between 50 and 405 K. The spectra exhibit up to six separated peaks at high temperatures, which are depicted in detail for both compounds at 375 and 200 K in Fig. 15 in the Appendix. The peaks broaden and overlap when decreasing the temperature. At temperatures below 80 K only a single broad peak is observed which is associated with the onset of static

TABLE I. Probability for the various possible numbers of nearest-iron neighbors assuming a random Fe-Li distribution.

No. of Fe neighbors	0	1	2	3	4	5	6	7	8
Probability [%]	3.9	15.6	27.3	27.3	17.1	6.8	1.7	0.2	0.0

antiferromagnetic correlations and the antiferromagnetic order observed below 50 K.

The appearance of satellite peaks as evinced in Fig. 15 can have two reasons: (1) The separated peaks at high temperatures originate from different local magnetic field values due to different numbers and geometries of nearest-neighbor *paramagnetically polarized* Fe ions in the Li/Fe disordered lattice. This scenario is discussed above for the zero-field Mössbauer spectra in the magnetically ordered state below 50 K. (2) An alternative interpretation based on electric-quadrupole hyperfine interaction would produce, in a powder sample for a nuclear spin $I = 3/2$, a central peak accompanied by four equally spaced singularities. The inner two of these singularities would look like horn-shaped, asymmetric peaks, and the two outer singularities would appear as a step-shaped decrease in intensity [26]. For the materials studied at hand, this is not observed at high temperatures (see Figs. 9 and 15). Even considering different Li sites with different quadrupolar coupling constants would most likely not result in the observed spectral peaks. For explaining at least five of the six observed line patterns, two different electric field gradients (EFGs) would have to be present with one being approximately twice as large as the other. Such a large difference in the EFG in one compound is indeed difficult to justify. Moreover, the intensity of the single peaks increases with decreasing temperature and the spectra become asymmetric at low temperatures (see, e.g., the spectra at 292 K and below), whereas any quadrupolar splitting is expected to be symmetric around the central

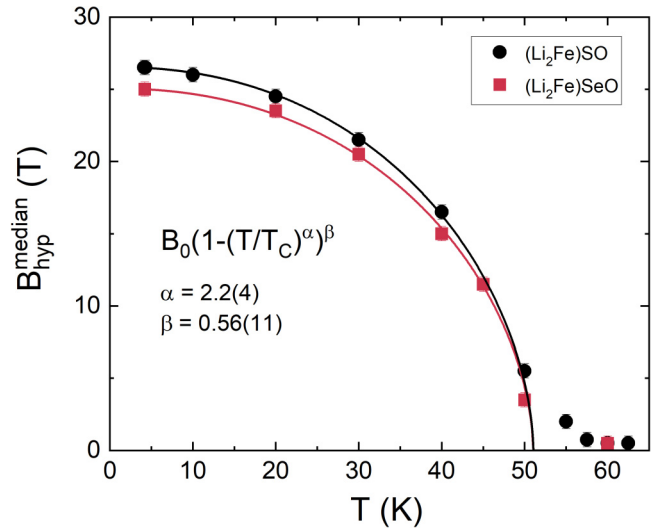

FIG. 8. Temperature dependence of the median magnetic hyperfine field $B_{\mathrm{hyp}}^{\mathrm{median}}$ for $(Li_2Fe)SO$ (black squares) and $(Li_2Fe)SeO$ (red dots). The solid lines describe a phenomenological model $B_{\mathrm{hyp}}^{\mathrm{median}} = B_0[1 - (\frac{T}{T_C})^{\alpha}]^{\beta}$ with shared T_C, α, and β (see the text).

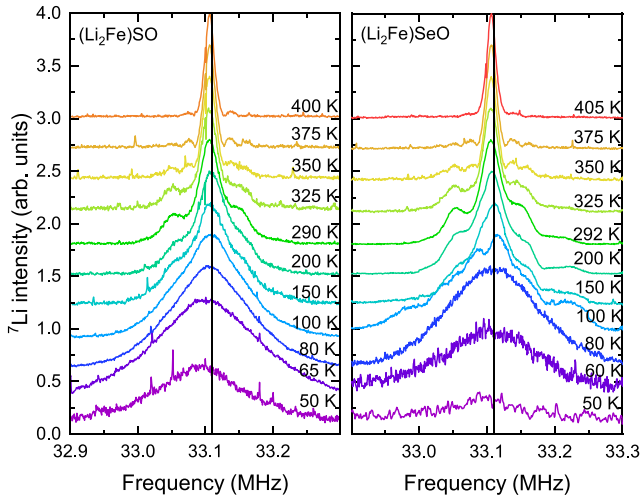

FIG. 9. The ^{7}Li NMR spectra of $(Li_2Fe)SO$ (left) and $(Li_2Fe)SeO$ (right) for different temperatures between 50 and 405 K in a static magnetic field of $2.001T$. Note the five satellite lines resolved at 350 and 375 K associated with different numbers of next-nearest-neighbor Fe ions (see discussion in the text). The solid line represents the unshifted resonance frequency of ^{7}Li with $\gamma = 16.5471$ MHz/T at this magnetic field.

resonance line, and the intensity of the quadrupolar peaks is not expected to increase with decreasing temperature. Therefore, we conclude that the first scenario is more appropriate.

The probability distribution for the number of nearest-neighbor Fe ions for a stochastic Fe-Li distribution is shown in Table I. This distribution indeed suggests six to seven different Li environments, such as, e.g., seen in the NMR spectra between 200 and 375 K. Note that in NMR at this elevated temperatures we study a *paramagnetically polarized* Fe spin environment in a powder sample. The internal field distribution is very different from the field distribution in the *antiferromagnetically ordered zero-field measurements* in Mössbauer spectroscopy. Qualitatively, the high-temperature NMR measurements are consistent with the low temperature Mössbauer results.

We determined the Knight shift from the frequency of the central peak maximum of each spectrum and the linewidth as the full width at half maximum (FWHM) from this peak. Due to the presence of multiple peaks, which gain intensity and broaden with decreasing temperature, below 200 K the side peaks contribute to the FWHM of the central peak. In the Appendix we present a comparison with the results of an alternative analysis, in which we determined the Knight shift from the center of gravity (COG) of the full spectra, and the linewidth from the square root of the second moment σ of the full spectra (see Fig. 16 and the text). This approach takes into account the contribution of satellite peaks. However, both approaches give qualitatively consistent results.

The temperature dependence of the linewidth and the Knight shift are shown in Fig. 10. The Knight shift is nearly temperature independent between 405 and 100 K. Below $\approx$100 K, K decreases strongly which signals the onset of antiferromagnetic correlations between the Fe electronic spins.

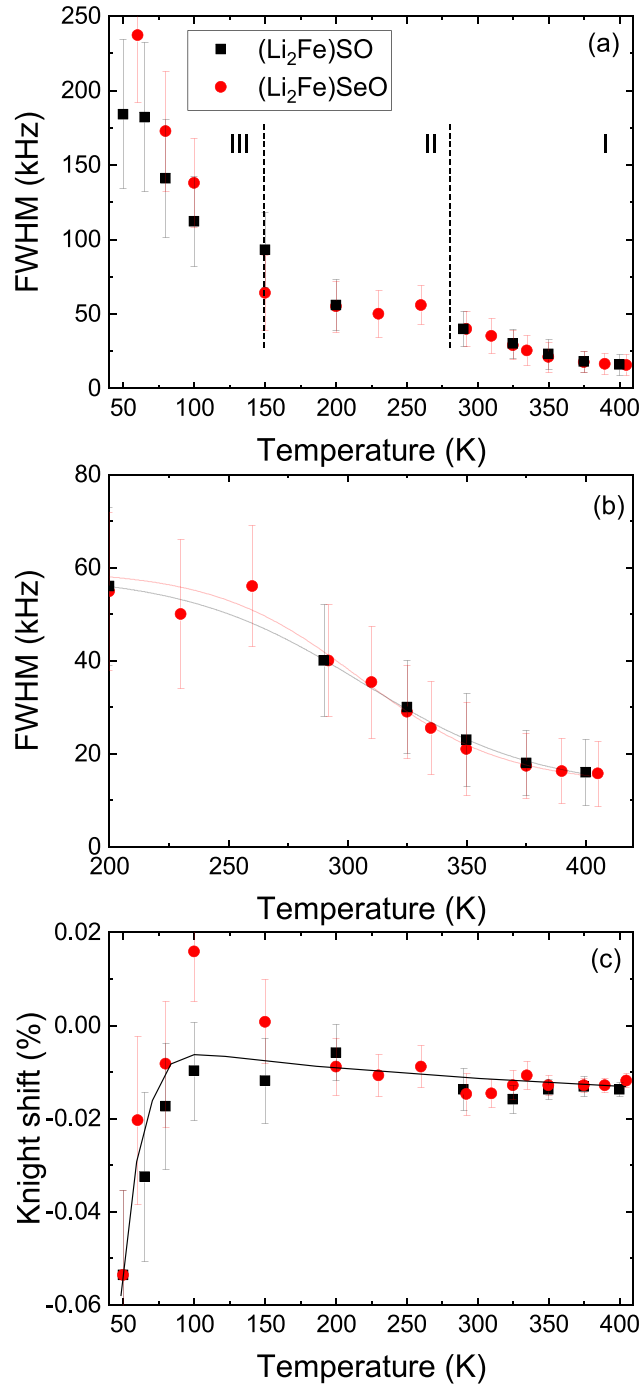

FIG. 10. (a) FWHM linewidth of the NMR spectra. The dashed lines separate the different temperature ranges mentioned in the text. (b) High-temperature part from panel (a) with a fit to the temperature dependence of the linewidths to Eq. (3). (c) Knight shift determined from the central peak maximum (open symbols) with a line as a guide to the eye.

Regarding the NMR linewidth, we identify three temperature ranges of interest: (I) an increase of the linewidth with decreasing temperature between 400 and 280 K [enlarged in Fig. 10(b)], (II) a constant linewidth between 280 and about 150 K, and (III) a strong increase of the linewidth between

150 and 50 K. Both compounds, $(Li_2Fe)SO$ and $(Li_2Fe)SeO$ behave very similarly.

The T dependence of the linewidth in range (I) can most likely be explained by motional narrowing, where the thermally activated hopping of the Li ions averages out the hyperfine fields at the Li nucleus and lead to a narrow linewidth of about 15 kHz at 400 K. Note, that this linewidth is still a factor of ≈10 larger compared with other nonmagnetic Li-ion battery materials [27–29]. We attribute this to the magnetic moments of the Fe ions, which generate a large hyperfine field at the Li nucleus even at high temperatures in comparison with nonmagnetic Li-ion battery materials, where the linewidth is caused by ^{7}Li homonuclear dipolar broadening of the nuclear spins.

The Fe magnetic moments do not affect the hopping of Li ions itself but increase the linewidth of the NMR spectra. Since the side peaks also vanish above 400 K, we assume that the hopping rate of all Li ions is faster than the linewidth, i.e., the inverse correlation time of the Li-ion hopping $\tau^{-1} \gg 15$ kHz (fast motional regime) above 400 K.

The onset temperature T_{onset} of the Li-ion hopping is the temperature that separates the Li diffusion regime (I) from the rigid-lattice linewidth regime (II), in which the linewidth has a constant value of ≈60 kHz. Below T_{onset}, all Li ions are immobile on the timescale of NMR. We estimate $T_{\text{onset}} \approx 280$ K. We can describe the temperature dependence of the linewidth in this transition with a phenomenological Fermi function (3). Here, $T_{\text{inflection}}$ marks the midpoint and A the width of the transition,

$$\Delta\nu(T) = \Delta\nu_{\text{rl}} - \frac{\Delta\nu_{\infty} - \Delta\nu_{\text{rl}}}{1 + \exp\left(\frac{T_{\text{inflection}} - T}{A}\right)}, \tag{3}$$

This analysis results in values of $T_{\text{inflection}} = 305$ K, $\Delta\nu_{\text{rl}} = 59$ kHz, and $\Delta\nu_{\infty} = 13$ kHz for both compounds. The width of the transition is $A = 37 \pm 4$ K for $(Li_2Fe)SO$, and $A = 30 \pm 8$ K for $(Li_2Fe)SeO$. These parameters agree with the above-determined values, e.g., $T_{\text{onset}} \approx T_{\text{inflection}} - A/2$, and the linewidth determined from the spectra at 400 K corresponds to $\Delta\nu_{\infty}$.

According to Waugh and Fedin [27,30] one can correlate the onset temperature T_{onset} to the activation energy E_a of the Li-ion diffusion process by

$$E_a\ (\text{eV}) \sim 1.67 \times 10^{-3}\, T_{\text{onset}}\ (\text{K}), \tag{4}$$

which gives an approximate E_a value of 0.47 eV. This value is slightly higher than the value from DFT calculations (0.32 eV) [5] and comparable to other Li-ion battery materials [27,29,31–34].

Further cooling below ≈150 K leads to an additional broadening of the ^{7}Li spectra in range (III) which we attribute to slowing down of Fe spin fluctuations and subsequently appearance of static magnetic hyperfine fields at the Li sites, similar to ^{7}Li NMR in $LiNiO_2$ [31]. This marks the onset of short-range static magnetic order, which cannot be distinguished from long-range magnetic order setting below 50 K. Due to the large linewidth the NMR spectra in the ordered state do not reveal detailed information in the Li or Fe site disordered compounds $(Li_2Fe)SO$ and $(Li_2Fe)SeO$.

2. Spin-spin relaxation

In Li-ion battery materials, in the slow motion regime, where $\omega_L \tau_c > 1$ with ω_L and τ_c being the nuclear Larmor frequency and the Li diffusion rate, respectively, the spin-spin relaxation rate T_2^{-1} typically follows the temperature dependence of the linewidth [27,35]. In this temperature range the NMR linewidth reflects the static distribution of local fields, and the nuclear spins start to dephase in these local fields over time. Therefore, as temperature decreases and motion slows down, the linewidth and T_2^{-1} increase in a correlated way. However, as can be seen in Fig. 11, for the materials studied in this work this holds only for temperatures above 350 K.

Below 350 K, T_2^{-1} decreases with decreasing temperature, whereas the linewidth continues to increase (see Fig. 10). Furthermore, indications for an oscillatory behavior set in in the recovery curves $M_{xy}(\tau)$ vs τ below about 300 K [see Figs. 11(c) and 11(d)]. Such oscillations in nuclear spin-spin relaxation can be caused by interaction with a very small static internal or external magnetic field. We therefore fit the relaxation of the nuclear magnetization to the following equation [36–38]:

$$M_{xy}(\tau) = M_0 \exp\left[-(2\tau)/T_2\right]\left[1 + F\cos\left(2\omega_{\text{int}}\tau - \phi\right)\right], \tag{5}$$

where M_0 is the initial nuclear magnetization, τ is the separation time between the 90° and the 180° pulses, T_2 is the nuclear spin-spin relaxation time, $\omega_{\text{int}} = {}^7\gamma B_{\text{int}}$ is the frequency of oscillations, and ϕ its phase shift. The prefactor F determines the relative strength of the oscillatory component in the transverse magnetization $M_{xy}(\tau)$. F is reduced if the internal field B_{int} is distributed, i.e., all nuclei precess at slightly different frequencies. In fact, the recovery curves in Figs. 11(c) and 11(d) do not show a clean oscillatory behavior with several cycles but only one low-frequency cycle. This is primarily due to the overall short T_2, but also due to the reduction of F in a powder sample that is about 1/3 on the whole temperature range, where the oscillations can be observed. Note that other functions such as a Gaussian relaxation do not fit the data.

From the fits, we extract the internal magnetic exchange field B_{int} that is shown in Fig. 11(b). It amounts to $B_{\text{int}} \approx 0.15$ mT, which corresponds to a Larmor frequency of $\omega_{\text{int}} \approx 2.5$ kHz. This is well below the linewidth of the central transition at all temperatures. Therefore, this internal magnetic exchange field does not lead to line broadening but only to oscillations in the nuclear spin-spin relaxation.

The small internal field at the Li ions may arise from small magnetic Fe impurity clusters, as detected also in the macroscopic susceptibility and Mössbauer measurements (see above). This would agree with the fact that the oscillations are more clearly visible in the S sample than in the Se sample [compare Figs. 11(c) and 11(d), and the larger error bars in the fit results for the Se sample], because the impurity content of the S samples seems to be larger than for Se. Despite the fact that the fits are not very accurate and the error bars are relatively large, the observed internal magnetic field of only 0.15 mT could well be explained by a minor phase of ferromagnetic impurities.

The appearance of a small static internal magnetic field could also explain the decrease of T_2^{-1} below 350 K. In

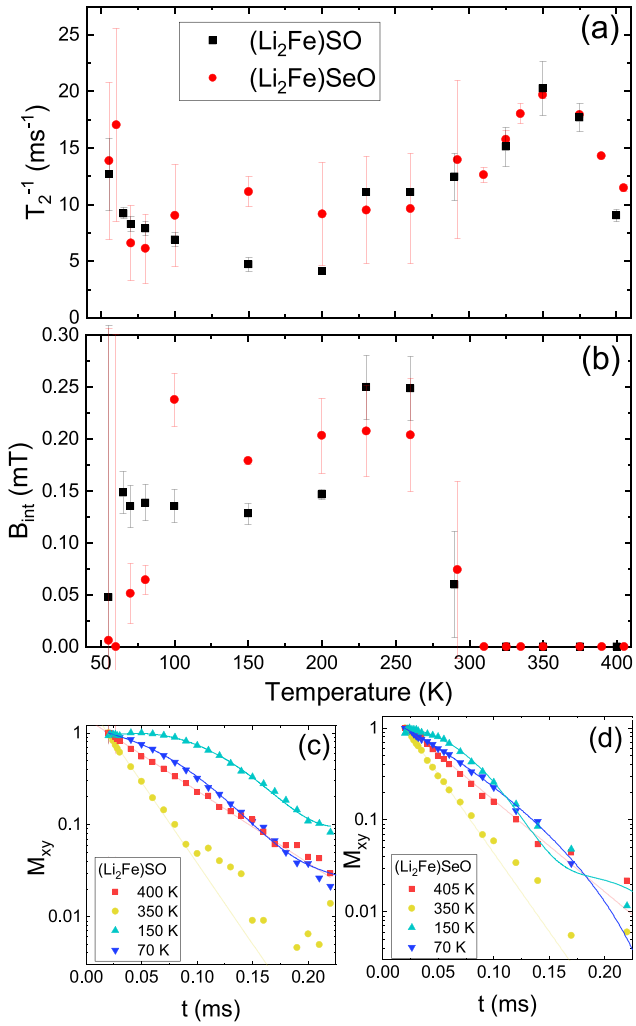

FIG. 11. (a) T_2^{-1} for $(Li_2Fe)SO$ (black squares) and for $(Li_2Fe)SeO$ (red circles) versus temperature. (b) Internal field B_{int} determined from Eq. (5). (c) Spin-echo decay of M_0 versus τ for $(Li_2Fe)SO$ and (d) for $(Li_2Fe)SeO$.

the motional narrowing regime, T_2^{-1} is dominated by fast fluctuations of the local fields, i.e., by fast motion of the Li ions. If the fluctuations slow further below 350 K, they might enter a regime where they no longer efficiently contribute to transverse relaxation, causing T_2^{-1} to decrease while the linewidth still broadens due to a broader distribution of static or quasistatic local fields. This could indicate a crossover from a fast fluctuating regime to a more inhomogeneous static-like regime. The emergence of oscillatory behavior in $M_{xy}(t)$ suggests the onset of local static fields from the ferromagnetic impurity, causing the T_2 relaxation transitioning from fluctuation-driven to coherence-driven, where nuclear spins precess in quasistatic internal fields rather than relaxing due to fluctuating ones. This could reduce T_2^{-1} despite the further increase in linewidth. It also shows that the measurement of Li-ion diffusion by NMR in battery materials containing magnetic ions can be difficult and does not always lead to unambiguous results.

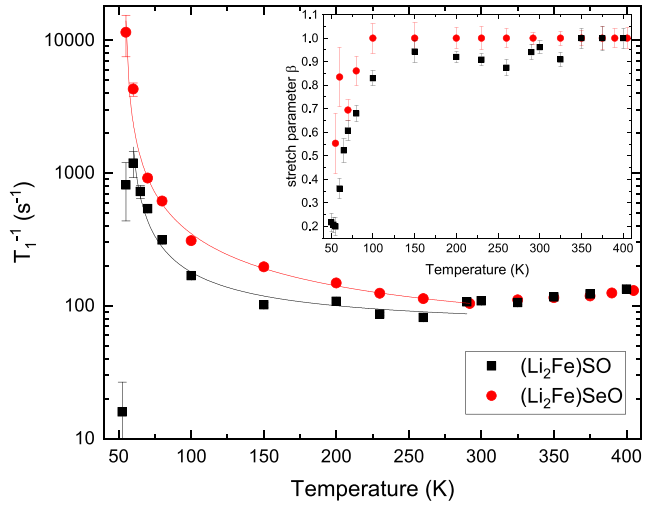

FIG. 12. T_1^{-1} for $(Li_2Fe)SO$ (black squares) and for $(Li_2Fe)SeO$ (red circles) versus temperature. The inset shows the exponent (stretching parameter) β. Lines are Curie-Weiss fits as described in the text in the temperature range 55 to 290 K for (Li2Fe)SeO and 60 to 290 K for (Li2Fe)SO, respectively.

3. Spin-lattice relaxation

The spin-lattice relaxation rate $1/T_1$ is determined by the magnetic hyperfine field amplitude oscillating with the nuclear Larmor frequency ω_L. In $(Li_2Fe)SO$ and $(Li_2Fe)SeO$ this amplitude is due to electronic spins of the nearest-neighbor Fe sites. $1/T_1$ measures the imaginary part of the dynamical spin susceptibility χ'' of the electronic spin system at ω_L:

$$(T_1T)^{-1} \propto \sum_{\vec{q},\alpha,\beta} F_{\alpha,\beta}(\vec{q}) \frac{\chi''_{\alpha,\beta}(\vec{q},\omega)}{\omega}. \tag{6}$$

Here, $F_{\alpha,\beta}(\vec{q})$ denotes the hyperfine form factors with $\alpha, \beta = x, y$ that are determined by the Fourier transformation of the hyperfine coupling tensor. If a system approaches a magnetic order, the dynamical spin susceptibility is enhanced, which leads to an enhancement of T_1^{-1} or $(T_1T)^{-1}$, respectively. Below the magnetic order transition, the spin fluctuations decrease again, and so does T_1^{-1}, leading to a maximum in T_1^{-1} at the magnetic ordering temperature.

For T_1^{-1} measured by NMR on powder samples, if the quadrupole splitting is not large and all transitions fall into one resonance line, the recovery function is given by $M_z(t) = M_0\{1 - f\exp[-(t/T_1)^\beta]\}$, where $f = 1$ for an ideal saturation of the nuclear magnetization M_0. β is a stretching parameter that describes a distribution of spin-lattice relaxation times, which often occurs in disordered systems, where nuclei located in different environments obey different relaxation times.

T_1^{-1} versus temperature is shown in Fig. 12 for $(Li_2Fe)SO$ and for $(Li_2Fe)SeO$. Similar to the linewidth data, we can identify three interesting temperature ranges: (i) an increase of T_1^{-1} between 290 and 400 K. This is most likely related to the onset of Li-ion diffusion, which induces additional relaxation through random fluctuation of local magnetic fields at the Li nucleus. In this temperature range, the relaxation

can be described by the Bloembergen, Purcell, Pound (BPP) model [35,39,40]

$$(T_1)^{-1} \propto \frac{\tau_c}{1+\omega_L^2\tau_c^2}, \tag{7}$$

where $\tau_c = \tau_0 \exp(E_a/k_BT)$ is the correlation time of the Li-ion motion which is coupled to the Li nuclear spin-lattice relaxation by dipolar interaction. E_a is the activation energy, which is the same as the activation energy determined above from the temperature dependence of the linewidth. In this model, the nuclear relaxation due to Li-ion motion exhibits a maximum if the condition $\omega_L\tau_c = 1$ is met. Since T_1^{-1} does not exhibit a maximum below 400 K, we conclude that the correlation time of the Li motion is larger than the inverse Larmor frequency in the measured temperature range, i.e., $\omega_L\tau_c \gg 1$.

We can use the activation energy $E_a = 0.47$ eV determined from the temperature dependence of the linewidth and estimate the correlation time τ_c at the inflection point $T_{\text{inflection}}$ from the rigid-lattice linewidth, $\tau_c(T_{\text{inflection}}) = 1/\Delta\nu_{\text{rl}} = 17 \times 10^{-6}$ s. This gives $\tau_0 = \tau_c(T_{\text{inflection}})/\exp(E_a/k_BT_{\text{inflection}}) = 3.14 \times 10^{-13}\ \text{s}^{-1}$. With this data, we estimate a maximum in T_1^{-1} at a temperature of $T_{\max} = (E_a/k_B)\ln[\tau_c(T_{\max})/\tau_0] = 475$ K, which is clearly above the measured temperature range up to 405 K. While our limited temperature range does not allow any conclusions about the type of Li-ion diffusion (continuum diffusion, jump diffusion, etc.) due to the missing maximum, it does explain the increase of T_1^{-1} above 290 K, which can be related to the diffusion of the Li ions.

Below 100 K the spin-lattice relaxation rate starts to increase. For $(Li_2Fe)SO$, T_1^{-1} exhibits a maximum at ≈60 K, which we identify as the onset of magnetic ordering, similar to the results of macroscopic susceptibility and Mössbauer spectroscopy. In contrast, T_1^{-1} of $(Li_2Fe)SeO$ continues to increase until the ^{7}Li signal disappears. This loss of signal intensity is visible in the NMR spectra in Fig. 9, where the noise level at 80 K is already much stronger for $(Li_2Fe)SeO$ compared with the spectra of $(Li_2Fe)SO$. At lower temperatures in the ordered state, when the spin-lattice relaxation rate is expected to slow down, static hyperfine field distributions in the Li/Fe site disordered systems could lead to such a broadening that one cannot obtain the spectra anymore. The disorder further contributes to the linewidth so that it is more and more difficult to obtain a reasonable signal. For $(Li_2Fe)SeO$, a phenomenological Curie-Weiss-fit $(T_1T)^{-1} = C/(T-\Theta)$ gives an ordering temperature of $\Theta = 54$ K [57 K for $(Li_2Fe)SeO$]. This value of Θ agrees with the temperature where the minimum in $\partial(\chi T)/\partial T$ is observed (see Fig. 3).

Another characteristics of the relaxation curves is a stretched exponential relaxation, which indicates a distribution of relaxation rates that can be described by a stretching exponent β in the relaxation function [41]. β is shown in the inset of Fig. 12. It is about 1 down to 100 K, which means no distribution of relaxation and all nuclei relax with the same T_1. Below 100 K, where short-range magnetic order sets in and leads to fluctuating hyperfine fields, β strongly decreases, indicating that different Li nuclei experience different levels of fluctuating hyperfine fields, which in turn agrees with the site disorder of Li and Fe atoms.

IV. FINAL DISCUSSION AND SUMMARY

We report magnetic susceptibility, magnetization, Mössbauer spectroscopy, and NMR studies on $(Li_2Fe)SeO$ and $(Li_2Fe)SO$. Our data reveal a Pauli paramagnetic-like behavior below 300 K, a long-range antiferromagnetically ordered ground state below ≈50 K and a regime of short-range magnetic correlations up to 100 K. This reflects the strong dilution of the paramagnetic iron ions on the TM site as well as the geometric frustration of the antiferromagnetic nearest-neighbor magnetic exchange interactions on the fcc TM sublattice with dominant triangular magnetic exchange geometry. Our results are consistent with a random Li-Fe distribution on the shared lattice position so that percolation effects must be taken into account. The 1/3 population of the TM site by magnetic iron only slightly exceeds the theoretical percolation threshold on a cubic lattice of ≃0.31 [42]. On the other hand, introducing nonmagnetic sites into the individually frustrated and highly degenerate kagome planes provides the random combination of frustrated and unfrustrated plaquettes which can favor long-range antiferromagnetic order as observed at hand, spin-glass behavior, or intriguing order-disorder phenomena [43,44]. The geometric frustration manifests itself also in a nonlinear saturation effect in the dependence of the ^{57}Fe magnetic hyperfine field on the number n of nearest-neighbor Fe ions in the long-range ordered state.

Depending on the local geometry of the occupied and unoccupied paramagnetic sites, magnetic frustration can be generated and lifted. This may yield the tendency to stabilize long-range magnetic order and to increase the ordering temperature. On the other hand, increasing dilution will weaken and eventually completely suppress long-range magnetic order when exceeding the percolation threshold for the given systems which has been shown for several related examples [45–48]. Our observation of two regimes of short- and long-range magnetic order in $(Li_2Fe)SeO$ and $(Li_2Fe)SO$ reflect these contrary tendencies.

Thermally activated Li-ion hopping is deduced by motional narrowing of the ^{7}Li NMR resonance line above approximately 250 K. From the temperature dependence of the linewidth, we estimate an activation energy of $E_a = 0.47$ eV. The onset of Li-ion motion also leads to an increase in the spin-lattice relaxation rate T_1^{-1} with increasing temperature. However, a maximum in T_1^{-1} could not be observed within the accessible temperature range of our experiment. The estimated activation energy is similar to values reported for other Li-ion battery materials, making lithium-rich antiperovskites a promising cathode material.

In general, our study elucidates magnetism in a disordered semimetallic system with geometric frustration and thermally induced ion diffusion dynamics.

ACKNOWLEDGMENTS

The authors gratefully acknowledge valuable discussion with Samuel Coles, Jochen Geck, Martin Valldor, and Maurits Haverkort. Work has been done in the framework of the joint project KL 1824/20-1 & GR 5987/2-1 funded by Deutsche Forschungsgemeinschaft (DFG). Technical support, and discussions within the DFG Research Training Group

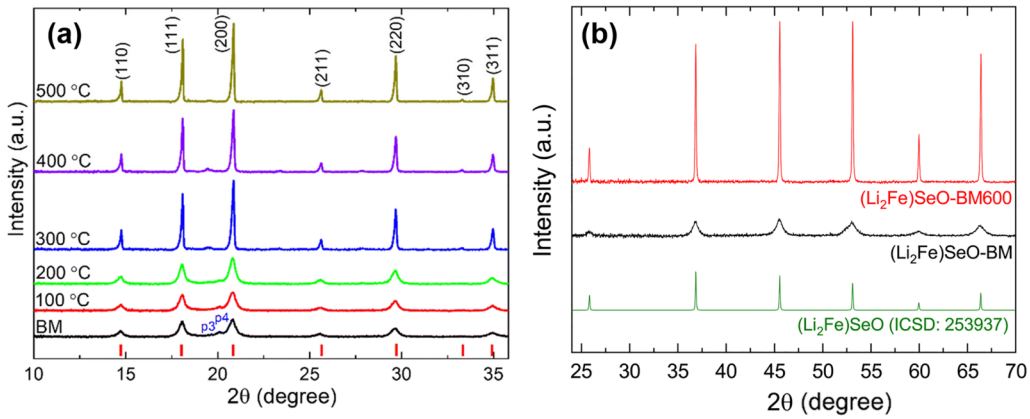

FIG. 13. X-ray diffraction patterns of the investigated samples. (a) $(Li_2Fe)SO$, reprinted from Ref. [18]. The red tick marks indicate the expected Bragg reflections for the ideal $(Li_2Fe)SO$ phase; secondary phases are labeled in blue. (b) $(Li_2Fe)SeO$, reprinted from Ref. [20], along with the reference pattern for the $(Li_2Fe)SeO$.

Mixed Ionic Electronic Transport (GRK 2948) are gratefully acknowledged. F.S. and H.-H.K. acknowledge funding by the DFG collaborative research center SFB 1143 "Correlated Magnetism: From Frustration to Topology." Work has also been supported within the framework of the Excellence Strategy of the Federal and State Governments of Germany via the Heidelberg University's flagship EMS initiative and the Cluster of Excellence STRUCTURES, and via the TU Dresden/U Würzburg Cluster of Excellence ct.qmat. M.A.A.M. thanks the IFW excellence program for financial support.

V. DATA AVAILABILITY

The data that support the findings of this article are openly available [49].

APPENDIX

1. Characterization by XRD

The XRD patterns shown of the samples under study and for different postsynthesis treatments in Fig. 13 confirm the main $(Li_2Fe)SO$ and $(Li_2Fe)SeO$ phases. The synthesis procedure of ball milling is known to produce materials with a significant amorphous fraction and broadened diffraction features which is reflected by the data. For a detailed discussion of the impurity phases please see our previous works Refs. [18,20].

2. Magnetization studies

Figure 14 displays magnetization curves of several samples under study with different postsynthesis treatment. As

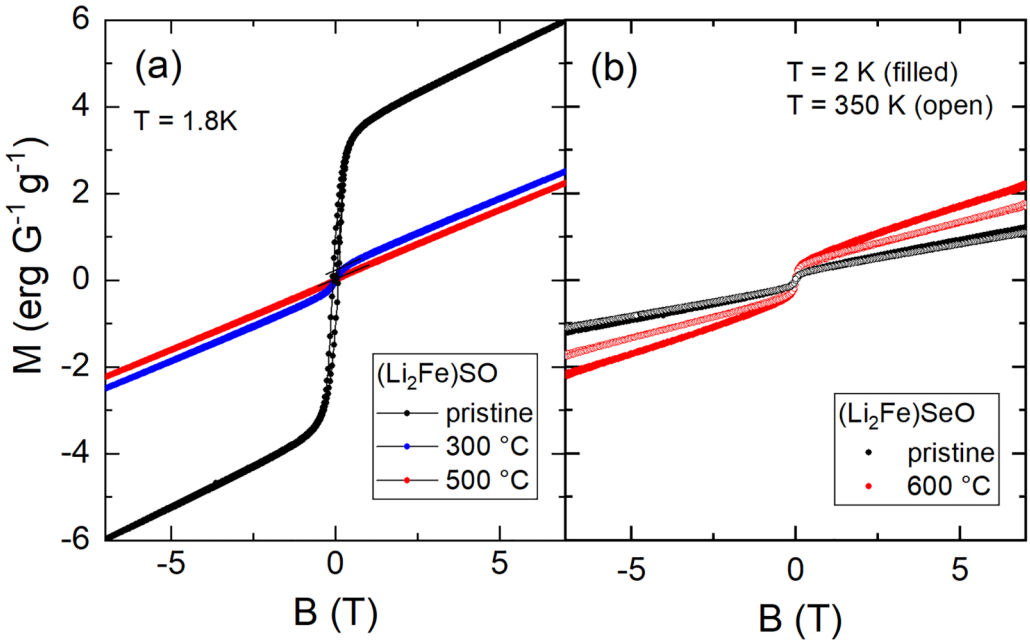

FIG. 14. Magnetization of various samples of (a) $(Li_2Fe)SO$ and (b) $(Li_2Fe)SeO$ vs external magnetic field at selected temperatures. The legend gives the temperature of postsynthesis heat treatment.

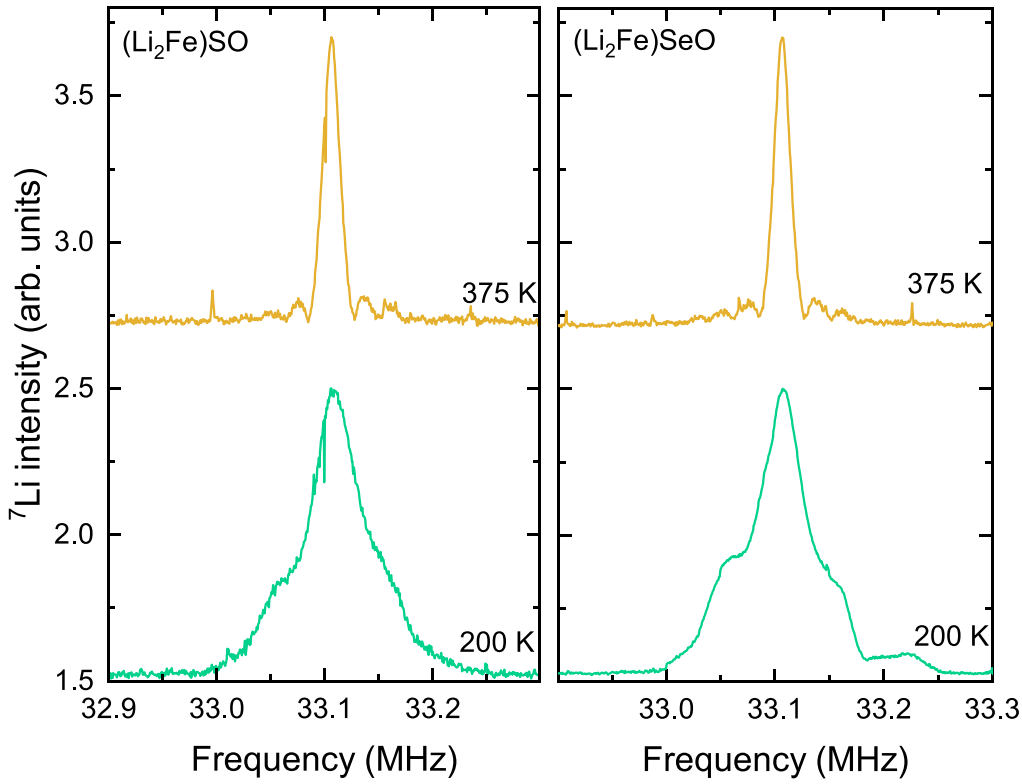

FIG. 15. The ^{7}Li NMR spectra of $(Li_2Fe)SO$ and $(Li_2Fe)SeO$ at 375 and 200 K.

shown in Fig. 14(a), postsynthesis heat treatment yields of the ferromagnetic impurity phases as shown by M vs B curves obtained at $T = 1.8$ K. While the amount of ferromagnetic impurities is much less in pristine $(Li_2Fe)SeO$ as compared with $(Li_2Fe)SO$, postsynthesis treatment does not suppress the ferromagnetic component(s). Measurements at 350 K show that the ferromagnetic component does not change visibly below room temperature. As discussed above, we attribute the ferromagnetic component to iron [$\approx$222 erg/(Gg)] and Fe_xS with $x \leqslant 1$ [typically $\approx 10 - 20$ erg/(Gg)] impurity phases. Attributing the major ferromagnetic response to iron would hence imply <2 w%, <0.1 w%, and <0.01 w% iron impurity phase in $(Li_2Fe)SO$ with no 300 °C and 500 °C postsynthesis heat treatment, while it would be <0.1 w% in both $(Li_2Fe)SeO$ materials under study.

3. Detail of the NMR spectra

Figure 15 shows the ^{7}Li NMR spectra of $(Li_2Fe)SO$ and $(Li_2Fe)SeO$ at 375 and 200 K. At high temperatures, the spectra show up to six separated peaks. The intensity of these additional peaks increases with decreasing temperature, and the all peaks broaden at lower temperature. Moreover, the spectra become asymmetric at low temperatures.

4. Comparison of two strategies to determine NMR linewidth and Knight shift

It is not straightforward to determine the linewidth ($\Delta\nu$) and the Knight shift (K) consistently for all temperatures. In the main text, We determined the Knight shift from the frequency of the central peak maximum of each spectrum and the linewidth as the full width at half maximum (FWHM) from this peak. Due to the presence of multiple peaks, which gain intensity and broaden with decreasing temperature, below 200 K the side peaks contribute to the FWHM of the central peak. On the other hand, if we read the linewidth from the central peak, we do not take into account the contribution of the side peaks to the spectra at high temperatures. Here, Fig. 16 present a comparison with the results of an alternative analysis, in which we determined the center of gravity (COG) of the full spectra and the square root of the second moment, σ, of the full spectra. Both approaches give qualitatively consistent results.

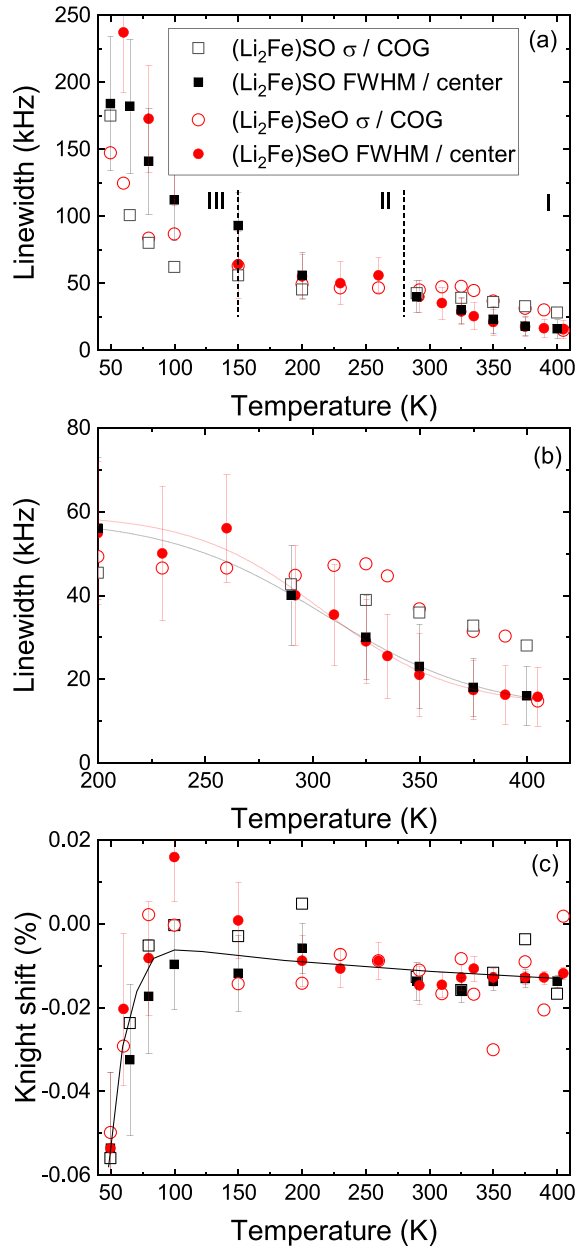

FIG. 16. (a) The linewidth of the NMR spectra. Closed symbols are determined from the center of gravity (COG) and the square root of the second moment, σ. Open symbols are read from the maximal peak (center frequency) and the full width at half maximum (FWHM). Black symbols are for $(Li_2Fe)SO$, red ones for $(Li_2Fe)SeO$. The dashed lines separate the different temperature ranges mentioned in the text. (b) Detail of the high-temperature part from panel (a) with a fit to the temperature dependence of the linewidths (FWHM of center peaks) to Eq. (3). (c) Knight shift from COG (closed symbols) and maximal peak (open symbols) with a line as a guide to the eye.

[1] A. Manthiram, A reflection on lithium-ion battery cathode chemistry, Nat. Commun. **11**, 1550 (2020).

[2] J. Du, Q. Li, J. Chai, L. Jiang, Q. Zhang, N. Han, W. Zhang, and B. Tang, Review of metal oxides as anode materials for lithium-ion batteries, Dalton Trans. **51**, 9584 (2022).

[3] J. Zheng, B. Perry, and Y. Wu, Antiperowskite superionic conductors: A critical review, ACS Mater. Au **1**, 92 (2021).

[4] K. T. Lai, I. Antonyshyn, Y. Prots, and M. Valldor, Anti-perovskite Li-battery cathode materials, J. Am. Chem. Soc. **139**, 9645 (2017).

[5] Z. Lu and F. Ciucci, Anti-perovskite cathodes for lithium batteries, J. Mater. Chem. A **6**, 5185 (2018).

[6] Z. Deng, D. Ni, D. Chen, Y. Bian, S. Li, Z. Wang, and Y. Zhao, Anti–perovskite materials for energy storage batteries, InfoMat **4**, e12252 (2021).

[7] C. Wang and J. Hong, Ionic/electronic conducting characteristics of $LiFeFO_4$ cathode materials: The determining factors for high rate performance, Electrochem. Solid-State Lett. **10**, A65 (2007).

[8] R. Malik, D. Burch, M. Bazant, and G. Ceder, Particle size dependence of the ionic diffusivity, Nano Lett. **10**, 4123 (2010).

[9] M. Reynaud, J. Serrano-Sevillano, and M. Casas-Cabanas, Imperfect battery materials: A closer look at the role of defects in electrochemical performance, Chem. Mater. **35**, 3345 (2023).

[10] C. Rudisch, H.-J. Grafe, J. Geck, S. Partzsch, M. v. Zimmermann, N. Wizent, R. Klingeler, and B. Büchner, Coupling of Li motion and structural distortions in olivine $LiMnPO_4$ from ^{7}Li and ^{31}P NMR, Phys. Rev. B **88**, 054303 (2013).

[11] J. Werner, C. Neef, C. Koo, S. Zvyagin, A. Ponomaryov, and R. Klingeler, Antisite disorder in the battery material $LiFePO_4$, Phys. Rev. Mater. **4**, 115403 (2020).

[12] D. Ranaut, J. Kumar, and K. Mukherjee, Anti-site disorder driven short-range order and canted antiferromagnetism in inverse spinel $LiNiVO_4$, J. Magn. Magn. Mater. **578**, 170833 (2023).

[13] D. Goonetilleke, B. Schwarz, H. Li, F. Fauth, E. Suard, S. Mangold, S. Indris, T. Brezesinski, M. Bianchini, and D. Weber, Stoichiometry matters: correlation between antisite defects, microstructure and magnetic behavior in the cathode material $Li_{1-z}Ni_{1+z}O_2$, J. Mater. Chem. A **11**, 13468 (2023).

[14] Z. Zeng, H. Lei, X. Lu, C. Zhu, Y. Wen, J. Zhu, X. Ji, W. Sun, Y. Yang, and P. Ge, Li-fe anti-sites defects in $LiFePO_4$: Mechanism, characterization and cathode-regeneration applications, Energy Storage Mater. **74**, 103947 (2025).

[15] S. W. Coles, V. Falkowski, H. S. Geddes, G. E. Pérez, S. G. Booth, A. G. Squires, C. O'Rourke, K. McColl, A. L. Goodwin, S. A. Cussen, S. J. Clarke, M. S. Islam, and B. J. Morgan, Anion-polarisation-directed short-range-order in antiperovskite Li_2FeSO, J. Mater. Chem. A **11**, 13016 (2023).

[16] Z. Deng, D. Chen, M. Ou, Y. Zhang, J. Xu, D. Ni, Z. Ji, J. Han, Y. Sun, S. Li, C. Ouyang, and Z. Wang, Cation disordered anti-perovskite cathode materials with enhanced lithium diffusion and suppressed phase transition, Adv. Energy Mater. **13**, 2300695 (2023).

[17] H. K. Singh, I. Samathrakis, N. Fortunato, J. Zemen, C. Shen, O. Gutfleisch, and H. Zhang, Multifunctional antiperovskites driven by strong magnetostructural coupling, npj Comput. Mater. **7**, 98 (2021).

[18] M. A. A. Mohamed, H. A. A. Saadallah, I. G. Gonzalez-Martinez, M. Hantusch, M. Valldor, B. Büchner, S. Hampel, and N. Gräßler, Mechanochemical synthesis of Li-rich $(Li_2Fe)SO$ cathode for Li-ion batteries, Green Chem. **25**, 3878 (2023).

[19] L. Singer, B. Dong, M. A. A. Mohamed, F. L. Carstens, S. Hampel, N. Gräßler, and R. Klingeler, Separating cationic and anionic redox activity in the lithium-rich antiperovskite $(Li_2Fe)SO$, ACS Appl. Mater. Interfaces **16**, 40873 (2024).

[20] L. Singer, M. A. A. Mohamed, H. Hahn, I. G. Gonzalez-Martinez, M. Hantusch, K. Wenelska, E. Mijowska, B. Büchner, S. Hampel, N. Gräßler, and R. Klingeler, Elucidating the electrochemical reaction mechanism of lithium-rich antiperovskite cathodes for lithium-ion batteries as exemplified by $(Li_2Fe)SeO$, J. Mater. Chem. A **11**, 14294 (2023).

[21] S. Kamusella and H.-H. Klauss, Moessfit. A free Mössbauer fitting program, Hyperfine Interact. **237**, 82 (2016).

[22] D. Mikhailova, L. Giebeler, S. Maletti, S. Oswald, A. Sarapulova, S. Indris, Z. Hu, J. Bednarcik, and M. Valldor, Operando studies of antiperovskite lithium battery cathode material $(Li_2Fe)SO$, ACS Appl. Energy Mater. **1**, 6593 (2018).

[23] M. E. Fisher, Relation between the specific heat and susceptibility of an antiferromagnet, Philos. Mag. (1798–1977) **7**, 1731 (1962).

[24] S. Spachmann, P. Berdonosov, M. Markina, A. Vasiliev, and R. Klingeler, Linear magnetoelastic coupling and magnetic phase diagrams of the buckled-kagomé antiferromagnet $Cu_3Bi(SeO_3)_2O_2Cl$, Sci. Rep. **12**, 7383 (2022).

[25] R. Scheuermann, E. Roduner, G. Engelhardt, H.-H. Klauss, and D. Herlach, Antiferromagnetic ordering of magnetic moments due to cavity trapped electrons in sodium electrosodalite: A zero-field μSR study, Phys. Rev. B **66**, 144429 (2002).

[26] G. Lang, J. Bobroff, H. Alloul, P. Mendels, N. Blanchard, and G. Collin, Evidence of a single nonmagnetic Co^{3+} state in the Na_1CoO_2 cobaltate, Phys. Rev. B **72**, 094404 (2005).

[27] S.-H. Baek, L. M. Reinold, M. Graczyk-Zajac, R. Riedel, F. Hammerath, B. Büchner, and H.-J. Grafe, Lithium dynamics in carbon-rich polymer-derived SiCn ceramics probed by nuclear magnetic resonance, J. Power Sources **253**, 342 (2014).

[28] K. Nakamura, H. Ohno, K. Okamura, Y. Michihiro, T. Moriga, I. Nakabayashi, and T. Kanashiro, ^{7}Li NMR study on Li^+ ionic diffusion and phase transition in Li_xCoO_2, Solid State Ionics **177**, 821 (2006).

[29] A. Kuhn, P. Sreeraj, R. Pöttgen, H.-D. Wiemhöfer, M. Wilkening, and P. Heitjans, Li ion diffusion in the anode material $Li_{12}Si_7$: Ultrafast quasi-1D diffusion and two distinct fast 3D jump processes separately revealed by ^{7}Li NMR relaxometry, J. Am. Chem. Soc. **133**, 11018 (2011).

[30] J. S. Waugh and E. I. Fedin, Relaxation effects in nuclear magnetic resonance, Sov. Phys. Solid State **4**, 1633 (1963).

[31] K. Nakamura, H. Ohno, K. Okamura, Y. Michihiro, I. Nakabayashi, and T. Kanashiro, On the diffusion of Li^+ defects in $LiCoO_2$ and $LiNiO_2$, Solid State Ionics **135**, 143 (2000).

[32] V. W. J. Verhoeven, I. M. de Schepper, G. Nachtegaal, A. P. M. Kentgens, E. M. Kelder, J. Schoonman, and F. M. Mulder, Lithium dynamics in $LiMn_2O_4$ probed directly by two-dimensional ^{7}Li NMR, Phys. Rev. Lett. **86**, 4314 (2001).

[33] O. Pecher, J. Carretero-González, K. J. Griffith, and C. P. Grey, Materials' methods: NMR in battery research, Chem. Mater. **29**, 213 (2017).

[34] C. Neef, A. Reiser, E. Thauer, and R. Klingeler, Anisotropic ionic conductivity of $LiMn_{1-x}Fe_xPO_4$ $(0 \leqslant x \leqslant 1)$ single crystals, Solid State Ionics **346**, 115197 (2020).

[35] P. Heitjans and J. Kärger, *Diffusion in Condensed Matter: Methods, Materials, Models* (Springer Science & Business Media, Berlin Heidelberg, 2006).

[36] A. Lombardi, M. Mali, J. Roos, and D. Brinkmann, Hyperfine fields at the Ba site in the antiferromagnet $YBa_2Cu_3O_{6.05}$, Phys. Rev. B **53**, 14268 (1996).

[37] S. Strässle, B. Graneli, M. Mali, J. Roos, and H. Keller, Absence of orbital currents in superconducting $YBa_2Cu_4O_8$ using

a Zeeman-perturbed nuclear-quadrupole-resonance technique, Phys. Rev. Lett. **106**, 097003 (2011).

[38] F. Bougamha, S. Selter, Y. Shemerliuk, S. Aswartham, A. Benali, B. Büchner, H.-J. Grafe, and A. P. Dioguardi, ^{31}P NMR investigation of quasi-two-dimensional magnetic correlations in $T_2P_2S_6$ (T = Mn, Ni), Phys. Rev. B **105**, 024410 (2022).

[39] N. Bloembergen, E. M. Purcell, and R. V. Pound, Relaxation effects in nuclear magnetic resonance absorption, Phys. Rev. **73**, 679 (1948).

[40] H. Buschmann, J. Dölle, S. Berendts, A. Kuhn, P. Bottke, M. Wilkening, P. Heitjans, A. Senyshyn, H. Ehrenberg, A. Lotnyk, V. Duppel, L. Kienle, and J. Janek, Structure and dynamics of the fast lithium ion conductor "$Li_7La_3Zr_2O_{12}$", Phys. Chem. Chem. Phys. **13**, 19378 (2011).

[41] D. C. Johnston, Stretched exponential relaxation arising from a continuous sum of exponential decays, Phys. Rev. B **74**, 184430 (2006).

[42] J. L. Bocquet, Percolative diffusion of a dumbbell interstitial defect on a fcc lattice: Calculation of a percolation threshold with use of a series method, Phys. Rev. B **50**, 16386 (1994).

[43] J. Villain, Insulating spin glasses, Z. Phys. B: Condens. Matter Quanta **33**, 31 (1979).

[44] E. Marinari, V. Martín-Mayor, and A. Pagnani, Spin-glass ordering in diluted magnetic semiconductors: A Monte Carlo study, Phys. Rev. B **62**, 4999 (2000).

[45] A. D. Beath and D. H. Ryan, Phase diagrams of site-frustrated Heisenberg models on simple cubic, bcc, and fcc lattices, Phys. Rev. B **73**, 214445 (2006).

[46] B. Jiang, B.-H. O, and J. T. Markert, Electronic, steric, and dilution effects on the magnetic properties of $Sm_{2-x}M_xCuO_{4-y}$ (M = Ce, Y, La, and Sr): Implications for magnetic pair breaking, Phys. Rev. B **45**, 2311 (1992).

[47] M. Hücker, V. Kataev, J. Pommer, J. Harraß, A. Hosni, C. Pflitsch, R. Gross, and B. Büchner, Mobility of holes and suppression of antiferromagnetic order in $La_{2-x}Sr_xCuO_4$, Phys. Rev. B **59**, R725 (1999).

[48] C. Yasuda, S. Todo, M. Matsumoto, and H. Takayama, Site-dilution-induced antiferromagnetic long-range order in a two-dimensional spin-gapped Heisenberg antiferromagnet, Phys. Rev. B **64**, 092405 (2001).

[49] F. Seewald, T. Schulze, N. Gräßler, F. Carstens, L. Singer, M. A. Mohamed, S. Hampel, B. Büchner, R. Klingeler, H.-H. Klauss, and H.-J. Grafe, Data repository for this work: https://opara.zih.tu-dresden.de/items/4c7fe390-0624-43aa-ad9a-443cd5bea7b4.